Synergistic induction of blood-brain barrier properties

Gergő Porko, Mária Mészáros, Anikó Szec, Fabien Gosselet, Ricardo Figuei, Ildikó Kálomista, Zsófia Hoyk, Gaszton Vizsnyiczai, Il Gróf, Jeng-Shi Jan, et al.

PNAS RESEARCH ARTICLE | NEUROSCIENCE

Synergistic induction of blood–brain barrier properties

Gergő Porkoláb[a,b], Mária Mészáros[a], Anikó Szecskó[a,b], Judit P. Vigh[a,b], Fruzsina R. Walter[a], Ricardo Figueiredo[c], Ildikó Kálomista[d], Zsófia Hoyk[a], Gaszton Vizsnyiczai[a], Ilona Grof[a], Jeng-Shiung Jan[e], Fabien Gosselet[f], Melinda K. Pirity[g], Monika Vastag[d], Natalie Hudson[h], Matthew Campbell[h], Szilvia Veszelka[a], and Mária A. Deli[a,1]

Edited by Jeremy Nathans, Johns Hopkins University School of Medicine, Baltimore, MD; received September 14, 2023; accepted April 5, 2024

Blood–brain barrier (BBB) models derived from human stem cells are powerful tools to improve our understanding of cerebrovascular diseases and to facilitate drug development for the human brain. Yet providing stem cell–derived endothelial cells with the right signaling cues to acquire BBB characteristics while also retaining their vascular identity remains challenging. Here, we show that the simultaneous activation of cyclic AMP and Wnt/β-catenin signaling and inhibition of the TGF-β pathway in endothelial cells robustly induce BBB properties in vitro. To target this interaction, we present a small-molecule cocktail named cARLA, which synergistically enhances barrier tightness in a range of BBB models across species. Mechanistically, we reveal that the three pathways converge on Wnt/β-catenin signaling to mediate the effect of cARLA via the tight junction protein claudin-5. We demonstrate that cARLA shifts the gene expressional profile of human stem cell–derived endothelial cells toward the in vivo brain endothelial signature, with a higher glycocalyx density and efflux pump activity, lower rates of endocytosis, and a characteristic endothelial response to proinflammatory cytokines. Finally, we illustrate how cARLA can improve the predictive value of human BBB models regarding the brain penetration of drugs and targeted nanoparticles. Due to its synergistic effect, high reproducibility, and ease of use, cARLA has the potential to advance drug development for the human brain by improving BBB models across laboratories.

blood–brain barrier | endothelial cell | signaling pathways | in vitro models | drug delivery

Significance

The blood–brain barrier (BBB) hinders drug delivery to the brain and is implicated in neurological diseases. To better understand these processes in humans, there is a need for culture models that mimic the complexity of the BBB. However, state-of-the-art human BBB models either suffer from a nonphysiological, mixed epithelial–endothelial identity or have weak barrier tightness, which greatly limits their usability. We identified a molecule combination that synergistically enhances barrier tightness in several in vitro models and induces complex BBB properties in human stem cell–derived endothelial cells by targeting a link between three signaling pathways. The molecule combination has the potential to improve BBB culture models across laboratories to advance both basic research and drug development for the human brain.

Endothelial cells (ECs) lining the smallest blood vessels in the brain possess unique anatomical and functional properties, collectively known as the BBB (1). Having specialized tight junction complexes, low rates of vesicular transcytosis, a negatively charged glycocalyx as well as efflux and influx transport systems, the BBB precisely controls the composition of the neural microenvironment (2). While these characteristics protect the brain from harmful substances, the barrier also prevents most drugs from entering the central nervous system, hindering drug development for neurological diseases (3). Additionally, BBB breakdown is a hallmark of a range of neuropathologies (4, 5), yet these processes are incompletely understood in humans at the molecular level. To provide mechanistic insight into BBB (dys)function and improve the prediction of drug delivery to the brain, there is a need for in vitro models that faithfully mimic the human BBB (6).

Culture models based on primary brain microvascular ECs isolated from animal tissue have been widely used as in vitro systems to study the BBB since the 1980s (7). However, there are major interspecies differences in the BBB proteome related to drug transport (8–10), which negatively impacts the translatability of findings from animal models to clinical trials. As a human alternative with good scalability, several BBB models have been established using induced pluripotent stem cells (11–21) or $CD34^+$ hematopoietic stem cells isolated from umbilical cord blood (22–25). Although these protocols represent major technological advances, state-of-the-art human BBB models either have high barrier tightness but suffer from a mixed epithelial–endothelial identity or are definitive vascular ECs with weak barrier properties (26, 27). In either case, the usability of these models is limited (26, 27).

To solve this problem, two-step differentiation has emerged as a promising strategy, in which stem cells are first differentiated into vascular ECs, and brain-like features are then induced in a second step (15, 21, 22). This is critical as BBB properties are not intrinsic to ECs but are promoted and maintained by organ-specific signaling cues from pericytes (28–30), astrocytes (31–33), and the microenvironment in vivo. While stem cell–derived vascular ECs are mostly responsive to inductive cues from coculture with pericytes or astrocytes (15, 21, 22), they need additional factors for proper junctional maturation and to acquire a complex BBB phenotype in vitro. Motivated by the unmet need for an approach that is efficient, reproducible, and easily adaptable by other laboratories, we focused on targeting developmentally relevant signaling pathways at the BBB using soluble factors.

Preprint Servers: The manuscript has been deposited to bioRxiv and is available under a CC-BY-NC-ND 4.0 International license at https://www.biorxiv.org/content/10.1101/2023.02.09.527899.

Competing interest statement: I.K. and M.V. are employed by the company Gedeon Richter. HUN-REN BRC has filed a patent (PCT/HU2023/050070) related to this work; G.P., M.M., A.S., S.V., and M.A.D. are named inventors. Other authors declare no competing interest. Hungarian national patent P2300053 was filed on 9 February 2023 by HUN-REN Biological Research Centre, Szeged, Hungary. Inventors are authors G.P., M.A.D., S.V., M.M., and A.S.

This article is a PNAS Direct Submission.

[1]To whom correspondence may be addressed. Email: deli.maria@brc.hu.

This article contains supporting information online at https://www.pnas.org/lookup/suppl/doi:10.1073/pnas.2316006121/-/DCSupplemental.

Published May 15, 2024.

During development, Wnt/β-catenin signaling controls brain angiogenesis (34–36) and BBB formation (37–39), and this pathway has been activated in vitro by Wnt ligands (Wnt-3a and Wnt-7a/b) or small molecules (LiCl, 6-BIO, and CHIR99021) to induce a subset of barrier properties (22, 40–43). Recently, TGF-β receptor antagonists (RepSox and A83-01) have also been shown to elevate junctional tightness in human stem cell–derived ECs (44, 45) via claudin-5, the dominant tight junction protein at the BBB. Notably, treatment with cyclic AMP-elevating agents (pCPT-cAMP, forskolin, and the cAMP-specific phosphodiesterase inhibitor Ro-20-1724) has previously been demonstrated to increase the resistance across bovine brain EC monolayers alone, and especially in combination with astrocyte-conditioned medium (46–48). Since astrocytes and their conditioned media can be a source of Wnt ligands (49, 50) and Wnt signaling-associated genes were reported to be induced by RepSox (44), we hypothesized that the cAMP, Wnt/β-catenin, and TGF-β pathways converge during BBB maturation, which can be leveraged to increase barrier properties in culture.

Here, we show that the simultaneous activation of cAMP and Wnt/β-catenin signaling while inhibiting the TGF-β pathway synergistically increases BBB tightness in ECs. Using our small-molecule cocktail containing pCPT-cAMP+Ro-20-1724+LiCl+A83-01, which we termed as cARLA, we demonstrate a simple and efficient approach to induce barrier properties in vitro that is reproducible across a range of BBB models from different species. We provide mechanistic insight into how these signaling pathways interact at the molecular level and illustrate how the complex phenotype induced by cARLA can potentially improve the prediction of drug and nanoparticle delivery across the human BBB.

Results

cARLA Synergistically Enhances BBB Tightness via Claudin-5. First, we performed an impedance-based screen of small molecules and recombinant proteins for their ability to enhance barrier tightness in cultured human stem cell–derived ECs (Fig. 1*A*). This approach allowed us to test selected activators of cAMP and Wnt as well as inhibitors of TGF-β signaling combinatorially in a 96-well plate format in real time (Fig. 1*B*). After optimizing treatment durations and concentrations (*SI Appendix*, Fig. S1 *A–F* and Table S1), we asked whether combining Wnt activation with TGF-β inhibition increases barrier integrity compared to targeting single pathways. Interestingly, we observed an increase but only by specific combinations, most effectively by LiCl+A83-01 (*SI Appendix*, Fig. S2 *A–H*).

We then asked whether Wnt activation by LiCl or TGF-β inhibition by A83-01 can potentiate the barrier integrity-promoting effect of cAMP signaling in ECs. Targeting the cAMP pathway alone by pCPT-cAMP supplemented with the cAMP-specific phosphodiesterase inhibitor Ro-20-1724 (cAMP+Ro) resulted in an immediate and potent increase in barrier integrity that diminished over time (Fig. 1*C* and *SI Appendix*, Fig. S3 *A* and *B*). The addition of either LiCl or A83-01 did not enhance the effect of cAMP+Ro (Fig. 1*C*). However, the combination of cAMP+Ro+LiCl+A83-01, which we termed as cARLA, synergistically elevated barrier integrity in ECs (Fig. 1*C*), i.e., the effect of cARLA was larger than the sum of its parts. This effect could be reproduced by other combinations that simultaneously activate cAMP and Wnt as well as inhibit TGF-β signaling (*SI Appendix*, Fig. S3 *C–E*), but we have found cARLA to be the most potent combination in our screen (Fig. 1*B* and *SI Appendix*, Fig. S3*E*). Added to this, the effect of cARLA on barrier integrity was long-lasting (>72 h) and resilient to withdrawal of treatment from ECs by replacing cARLA with control medium (Fig. 1*D* and *SI Appendix*, Figs. S3*E* and S4*A*).

We validated these findings in a BBB model in which human stem cell–derived ECs acquire brain-like characteristics (from now on referred to as brain-like ECs) upon coculture with pericytes (Fig. 1*E*) (22). Transendothelial electrical resistance (TEER) was synergistically increased upon cARLA treatment by 2.1-fold compared to the control group (Fig. 1*F* and *SI Appendix*, Fig. S4*B*), an effect that was highly reproducible across experiments (Fig. 1*G*). Moreover, we measured a lower permeability of tracers sodium fluorescein (2.2-fold) and Evans blue–albumin (7.4-fold compared to the control group) across the coculture model upon cARLA treatment (Fig. 1 *H* and *I*). As a proposed mediator of its barrier-tightening effect, cARLA elevated both the staining intensity (2.3-fold) and continuity (4.5-fold) of the tight junction protein claudin-5 at cell borders (Fig. 1 *J* and *K*). Importantly, similar results were obtained in EC monoculture (*SI Appendix*, Fig. S5 *A–F*), indicating that the effect of cARLA does not depend on other soluble factors from pericytes. We also confirmed the efficacy of cARLA treatment and its specificity for claudin-5 in an induced pluripotent stem cell–derived human BBB model with definitive vascular characteristics [EECM-BMEC-like cells (21), *SI Appendix*, Fig. S6 *A–K*].

To test whether the effect of cARLA is dependent on claudin-5, we assembled BBB models consisting of primary brain ECs, pericytes, and astrocytes isolated from wild-type (WT) mice or claudin-5 heterozygous (*Cldn5*$^{+/-}$) mice that have only one copy of *Cldn5* (Fig. 1*L*). Compared to WT cultures, *Cldn5*$^{+/-}$ cultures had 49% less claudin-5 at the protein level, which could be rescued by cARLA treatment (Fig. 1*M*). Similarly to human brain–like ECs and EECM-BMEC-like cells, cARLA not only increased the staining intensity of claudin-5 (Fig. 1*M*) but also its junctional localization (Fig. 1*N*) in both genotypes. TEER was elevated by cARLA compared to the control group in both genotypes, but approximately 50% less so in *Cldn5*$^{+/-}$ cultures (Fig. 1*O*), suggesting that cARLA increases TEER by inducing *Cldn5* gene expression.

We repeated the main experiments in additional, widely used BBB culture models of rodent origin to see whether the synergistic effect of cARLA is conserved between species. For this purpose, we selected the mouse brain EC line bEnd.3 in monoculture and a rat primary brain EC-pericyte-astrocyte coculture model (51), which considerably differ in their complexity (Fig. 2*A*). Barrier integrity measured by impedance was robustly elevated by cARLA in both models, albeit to a different extent and with different kinetics (Fig. 2 *B* and *C*). Notably, the optimal treatment concentrations of cARLA and its components were different between mouse bEnd.3 cells, primary rat brain ECs, and human brain–like ECs (*SI Appendix*, Table S1 and Figs. S7–S9). Therefore, we emphasize the need for optimizing these parameters first when testing cARLA in any BBB model. As validation, we measured a 2.1-fold increase in TEER (Fig. 2*D*) and decreased permeability of fluorescein (1.6-fold) and albumin (3.4-fold) tracers across bEnd.3 monolayers upon cARLA treatment (Fig. 2 *E* and *F*). In the rat primary coculture model, a 2.9-fold increase in TEER (Fig. 2*G*) as well as a 2.1-fold and 1.93-fold decrease in permeability was seen for fluorescein and albumin, respectively (Fig. 2 *H* and *I*). Similarly to human brain–like ECs, treatment with cARLA synergistically elevated the staining intensity of claudin-5 in both mouse bEnd.3 cells (Fig. 2*J*), and in rat primary brain ECs (Fig. 2*K*), but did not change the staining intensity of ZO-1 (*SI Appendix*, Figs. S7*G* and S8*G*). Taken together, our results reveal that cARLA synergistically enhances barrier tightness in a range of BBB models and this effect is dependent on claudin-5.

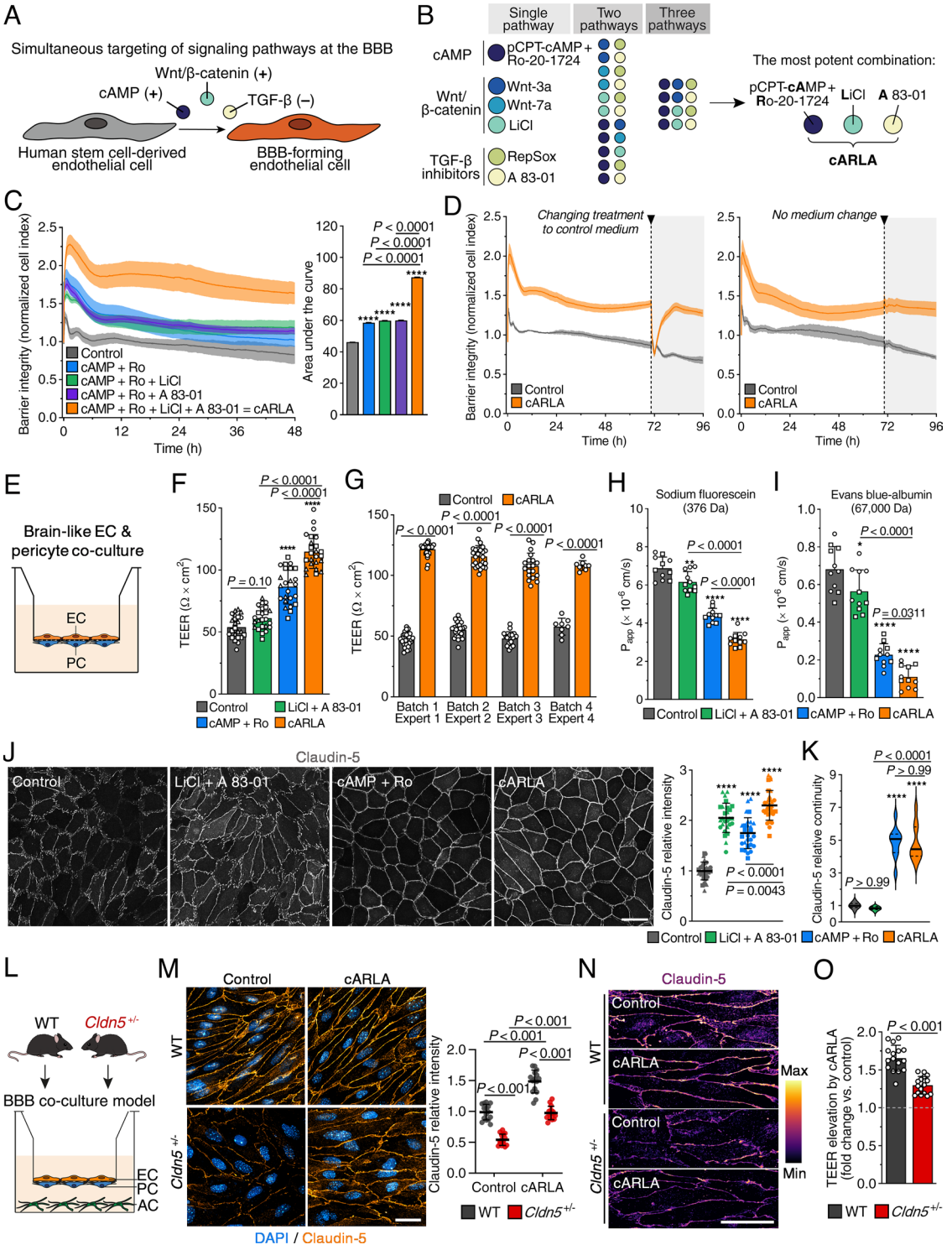

Fig. 1. cARLA synergistically enhances barrier tightness via claudin-5. (*A*) Rationale. (*B*) Schematic drawing of single compounds and their combinations tested in the impedance-based screen. (*C*) Barrier integrity of human cord blood stem cell–derived EC monolayers supplemented with PC-conditioned medium, measured by impedance. Higher normalized cell index values and a higher area under the curve indicate increased barrier integrity. Mean ± SD, ANOVA with Bonferroni's post hoc test, $^{****}P < 0.0001$ compared to the control group, $n = 6$. (*D*) Impedance kinetics of EC monolayers with or without changing cARLA treatment to control medium at 72 h. Mean ± SD, $n = 6$. (*E*) Schematic drawing of the BBB model: human stem cell–derived ECs acquire brain-like characteristics upon coculture with PCs. (*F*) Transendothelial electrical resistance (TEER) in the coculture model after 48 h treatment. Mean ± SD, ANOVA with Bonferroni's post hoc test, $^{****}P < 0.0001$ compared to the control group, $n = 24$ from three experiments. (*G*) Reproducibility of TEER measurements after 48 h cARLA treatment across experiments, measured by different experts using different batches of cells. Mean ± SD, ANOVA with Bonferroni's post hoc test, $n = 82$ from four experiments. (*H*) Permeability of sodium fluorescein and (*I*) Evans blue–albumin across the coculture model after 48 h treatment. P_{app}: apparent permeability coefficient. Mean ± SD, ANOVA with Bonferroni's post hoc test, $^{*}P < 0.05$, $^{**}P < 0.01$, $^{****}P < 0.0001$ compared to the control group, $n = 11$ from two experiments. (*J*) Claudin-5 immunostaining in human brain–like ECs. (Scale bar: 50 μm.) Mean ± SD for intensity and (*K*) median ± quartiles for continuity, ANOVA with Bonferroni's post hoc test, $^{****}P < 0.0001$ compared to the control group, $n = 27$ to 30 from three experiments. (*L*) Schematic drawing of BBB coculture models isolated from wild-type (WT) and *Cldn5*$^{+/-}$ mice. (*M* and *N*) Claudin-5 immunostaining in the mouse BBB coculture model. (Scale bar: 50 μm in both subpanels.) Mean ± SD, Two-way ANOVA with Bonferroni's post hoc test, $n = 15$. (*O*) Measurement of TEER in the mouse BBB coculture models. Values are presented as fold change (cARLA vs. control). Mean ± SD, unpaired *t* test, $t = 6{,}903$, $df = 30$, $n = 16$.

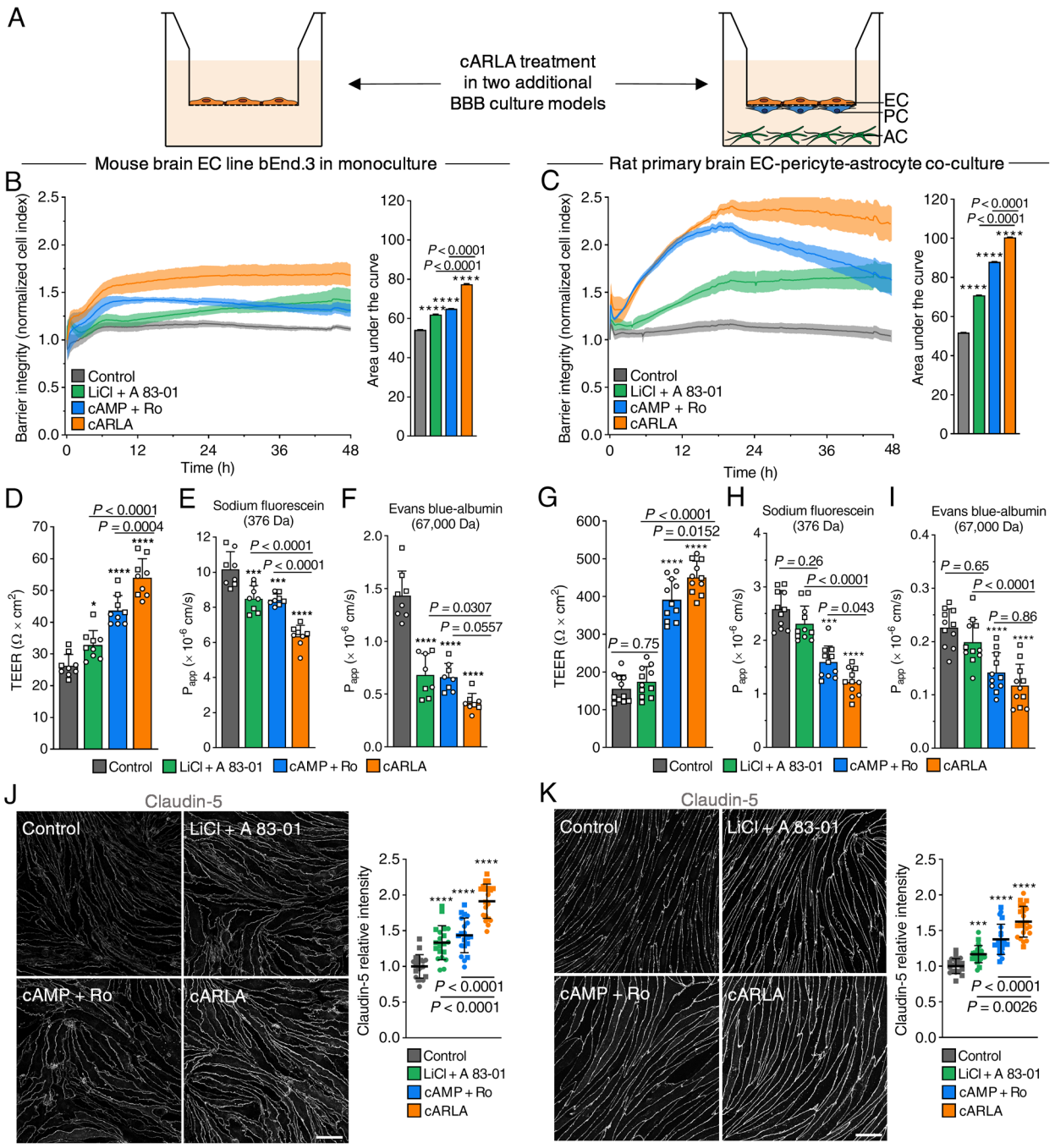

Fig. 2. The effect of cARLA on barrier tightness is reproducible in additional BBB culture models. (*A*) Schematic drawing of additional BBB culture models in which cARLA treatment was tested. (*B*) Real-time measurement of barrier integrity by impedance in mouse bEnd.3 cells and (*C*) in rat primary brain capillary ECs. Higher normalized cell index values and a higher area under the curve indicate increased barrier integrity. Mean ± SD, ANOVA with Bonferroni's post hoc test, ****$P < 0.0001$ compared to the control group, $n = 5$ to 6 for both panels. (*D*) Measurement of TEER as well as permeability of (*E*) sodium fluorescein and (*F*) Evans blue–albumin across mouse bEnd.3 monolayers after 48 h treatment. Similarly, (*G*) TEER as well as permeability of (*H*) sodium fluorescein and (*I*) Evans blue–albumin was measured across the rat primary cell–based coculture BBB model after 24 h treatment. Mean ± SD, ANOVA with Bonferroni's post hoc test, *$P < 0.05$, ***$P < 0.001$, ****$P < 0.0001$ compared to the control group, $n = 8$ in mouse bEnd.3 cells $n = 11$ in the rat primary BBB model from 2-2 experiments. (*J*) Claudin-5 immunostaining in mouse bEnd.3 cells and (*K*) in the rat primary BBB model. (Scale bar: 50 μm in both panels.) Mean ± SD, ANOVA with Bonferroni's post hoc test, ****$P < 0.0001$ compared to the control group, $n = 20$ to 22 from two experiments in both panels.

cARLA Promotes Barrier Maturation and Brain Endothelial Identity Revealed by MACE-Seq. To investigate gene expressional changes in human brain–like ECs upon cARLA treatment, we performed Massive Analysis of cDNA Ends (MACE-seq, Fig. 3*A*). Principal component analysis revealed a sharp separation of control and cARLA samples along principal component 1 (Fig. 3*B*). In line with our findings on barrier integrity, *CLDN5* was the most differentially expressed gene based on statistical significance (*SI Appendix*, Fig. S10*A*) among the 619 up-regulated and 546 down-regulated genes upon cARLA treatment (Fig. 3*C*). Key transcripts related to different aspects of BBB function were up-regulated by cARLA, such as *ABCB1* encoding the efflux pump P-glycoprotein, and *SLC2A1* encoding the glucose transporter GLUT1 (Fig. 3*C*). Conversely, genes involved in pathological BBB disruption, including *CCL2* (the C-C motif ligand-2 chemokine) and *SERPINE1* (plasminogen activator inhibitor-1) were down-regulated by cARLA (Fig. 3*C*).

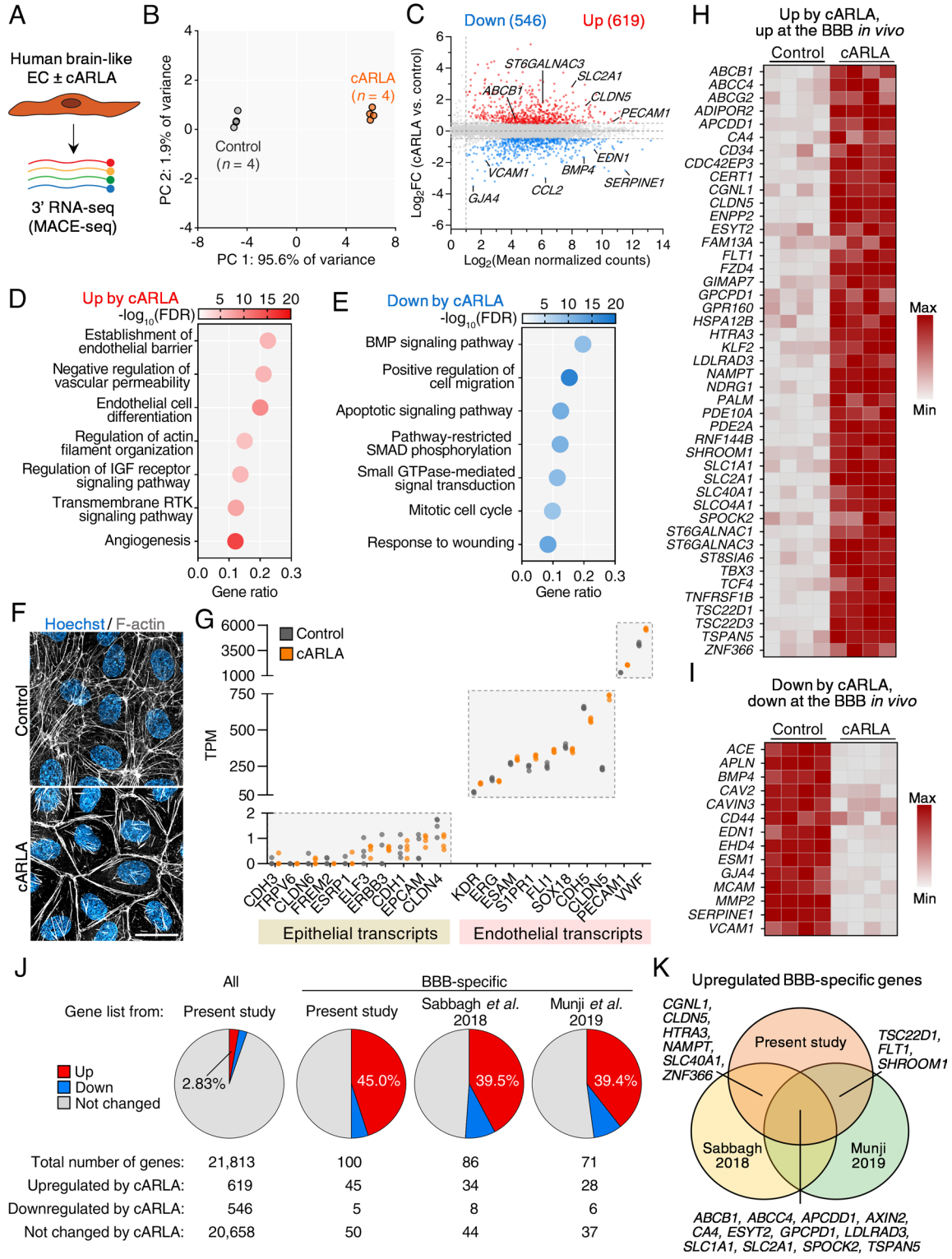

Fig. 3. cARLA promotes barrier maturation and brain endothelial identity in human brain–like ECs. (*A*) Schematic drawing of the experimental setup. (*B*) Principal component analysis (PCA) of control and cARLA-treated samples. (*C*) Mean-difference (MD) plot of cARLA vs. control samples showing up- and down-regulated genes and their expression levels. Key transcripts related to different aspects of BBB function are highlighted. (*D*) Functional enrichment analysis of up-regulated- and (*E*) down-regulated gene sets upon cARLA treatment. Gene Ontology Biological Process (GO:BP) terms are ranked based on their gene ratio and are colored based on statistical significance. (*F*) F-actin immunostaining, with or without cARLA treatment. (Scale bar: 40 μm.) (*G*) Validation of the vascular endothelial nature of human stem cell–derived brain-like ECs. Expression levels (TPM: transcript per million) of key epithelial and endothelial transcripts from our dataset are plotted on a three-segment y-axis covering multiple orders of magnitude. (*H*) Scaled heatmap of 45 BBB-specific genes that are up-regulated by cARLA and are enriched in brain ECs in vivo. (*I*) Scaled heat map of 14 genes that are down-regulated by cARLA and are enriched in peripheral ECs in vivo. (*J*) The ratio of up-regulated, not changed, and down-regulated genes by cARLA for all genes and BBB-specific genes using our and previously published (4, 52) lists. (*K*) Venn diagram of BBB-specific genes from the three lists up-regulated by cARLA.

On a pathway level, we observed an overrepresentation of genes related to EC differentiation and barrier formation as well as quiescence and maturation (Fig. 3 *D* and *E*). Accordingly, cARLA reduced the staining intensity of cytoplasmic vimentin fibers (*SI Appendix*, Fig. S11*A*), and the number of Ki-67$^+$ cells (*SI Appendix*, Fig. S11*B*) in EC monoculture. This was accompanied by a marked redistribution of F-actin from stress fibers to the cortical actin cytoskeleton (Fig. 3*F* and *SI Appendix*, Fig. S12*A*) and a more continuous ZO-1 staining at cell borders (*SI Appendix*, Fig. S12*B*), supporting the maturation of cell–cell contacts. Other up-regulated junctional genes include *F11R* (JAM-A), *CGNL1* (paracingulin/JACOP), and *PECAM1* (CD31; *SI Appendix*, Fig. S12 *C–E*).

Notably, the expression of key endothelial transcripts in human brain–like ECs was orders of magnitude higher than that of epithelial-associated transcripts (27), confirming the vascular endothelial nature of the model (Fig. 3*G*). To test whether cARLA further shifts the gene expression of ECs toward the in vivo brain EC signature, we examined a set of 100 transcripts (*SI Appendix*, Table S2 and Fig. S10*B*) that are enriched in brain *vs*. peripheral ECs in mice (4, 49, 52) and are robustly expressed at the human brain endothelium (53–56). We observed an upregulation of 45 BBB-specific genes by cARLA, including BBB-enriched transporters, enzymes, and transcription factors (Fig. 3*H*). By contrast, 14 BBB-depleted genes participating in cell–cell adhesion, proliferation, and vesicular transport, were down-regulated by cARLA (Fig. 3*I*). The ratio of BBB-specific genes up-regulated by cARLA was 45% according to our list of 100 genes, and 39.4-39.5% using two other published gene lists from mice (4, 52) (Fig. 3 *J* and *K* and *SI Appendix*, Table S3). This indicates that BBB-specific genes were 14 to 16× more likely to be up-regulated by cARLA compared to all genes (2.8% up-regulated, Fig. 3*J*). The effect of cARLA positively correlated with the gene pattern differences observed between mouse brain vs. peripheral ECs (52) but only partially matched the differences between mouse brain vs. lung ECs (4) (*SI Appendix*, Fig. S13*A*). Importantly, for BBB-specific genes, cARLA shifted the expression profile of human brain–like ECs in vitro toward values in ECs from isolated human brain microvessels (56) (*SI Appendix*, Fig. S13*B*). Together, these results demonstrate that cARLA promotes quiescence, barrier maturation, and the acquisition of a brain EC-like identity.

cARLA Induces a Complex BBB Phenotype at the mRNA, Protein, and Functional Levels. We verified our MACE-seq results at the protein and functional levels for four selected BBB properties in human brain–like ECs (also shown by category in *SI Appendix*, Fig. S14 *A–J*). First, genes encoding key enzymes that participate in the synthesis of the negatively charged EC glycocalyx, such as *ST6GALNAC1*, *ST6GALNAC3,* and *ST8SIA6*, were up-regulated by cARLA (Fig. 4*A*). This was also reflected by a higher intensity of wheat germ agglutinin (WGA) lectin staining, which recognizes negatively charged sialic acid residues in the glycocalyx, upon cARLA treatment (Fig. 4*B* and *SI Appendix*, Fig. S15*A*). Accordingly, we measured a more negative surface charge (Δ1.5 mV) in cARLA-treated ECs (Fig. 4*C*). Second, genes encoding BBB efflux transporters, such as P-glycoprotein (*ABCB1*), breast cancer–related protein (BCRP, *ABCG2*) and multidrug resistance-related protein 4 (MRP4, *ABCC4*), were up-regulated by cARLA (Fig. 4*D*). At the protein level, we observed a 20 to 35% elevation in the staining intensity of P-glycoprotein (Fig. 4*E* and *SI Appendix*, Fig. S16*A*) which was accompanied by a marked increase in its luminal–abluminal polarization in ECs treated with cARLA (*SI Appendix*, Fig. S16*B*). BCRP protein levels were also robustly induced by cARLA, especially in EC monoculture (*SI Appendix*, Fig. S16*B*). As a functional test of efflux pump activity, we measured the permeability of rhodamine 123, a ligand of efflux pumps, across the coculture model in blood-to-brain and brain-to-blood directions. The efflux ratio of rhodamine 123 was 2.1 upon cARLA treatment (a 1.6-fold increase compared to the control group), which could be reduced using verapamil, an efflux pump inhibitor (Fig. 4*F*). These results were also confirmed in accumulation assays using additional efflux pump ligands and inhibitors, with or without pericyte-conditioned medium (*SI Appendix*, Fig. S16 *D–G*). Together, our data reveal a higher glycocalyx density and better polarity and functionality of efflux pumps in ECs treated with cARLA.

On the other hand, genes associated with endocytic vesicle formation and nonspecific albumin uptake, suppressed pathways at the BBB in vivo, were also down-regulated by cARLA (Fig. 4*G*). In line with this and our results on albumin permeability (Fig. 1*I*), we observed 20 to 30% lower levels of albumin internalization in ECs upon cARLA treatment (Fig. 4 *H* and *I*). Moreover, the internalization process was sensitive to methyl-β-cyclodextrin, which inhibits lipid raft/caveolin-mediated endocytosis, but this effect was smaller in cARLA-treated cells (Fig. 4*I*). Finally, genes encoding cell adhesion molecules involved in leukocyte trafficking across the inflamed BBB, such as vascular cell adhesion molecule 1 (*VCAM1*) and E-selectin (*SELE*), showed a low expression at basal conditions (*SI Appendix*, Fig. S14*D*) and were down-regulated by cARLA (Fig. 4*J*). When challenged by a combination of TNF-α and IL-1β in increasing concentrations, both control and cARLA-treated ECs responded to cytokine treatment by a decrease in impedance (Fig. 4*K*). ECs treated with cARLA maintained a higher barrier integrity at lower cytokine concentrations, but a robust reduction in impedance was observed at the highest cytokine concentration, similarly to the control group (Fig. 4*K*). Treatment with proinflammatory cytokines also decreased barrier integrity in the BBB model both in control and cARLA groups, as measured by TEER (Fig. 4*L*), fluorescein (Fig. 4*M*), and albumin permeability (Fig. 4*N*). In agreement with this and our MACE-seq results, VCAM1 protein levels without TNF-α and IL-1β treatment were low in ECs and were decreased by cARLA (Fig. 4*O* and *SI Appendix*, Fig. S15*B*) but were robustly increased in both control and cARLA-treated ECs by proinflammatory cytokines (Fig. 4*O*). These findings suggest that cARLA-treated ECs have lower basal rates of endocytosis and retain their ability to respond to proinflammatory cytokines.

Targeted Pathways Converge on Wnt/β-Catenin Signaling to Mediate the Effect of cARLA. We then asked how the synergistic effect of cARLA on barrier tightness is orchestrated in brain-like ECs. Bioinformatic analyses using the STRING database revealed a network of interactions between the effector transcription factors of cAMP, Wnt, and TGF-β pathways, with β-catenin taking center stage (Fig. 5*A*). Indeed, we observed a robust induction of Wnt/β-catenin signaling-associated genes at the mRNA level (Fig. 5*B* and *SI Appendix*, Figs. S14*E* and S17*A*). In addition, both the staining intensity (Fig. 5 *C* and *D*) and nuclear accumulation of β-catenin (Fig. 5*E*) were synergistically elevated by cARLA, indicating a convergence of the targeted pathways on Wnt signaling. Active β-catenin levels were also increased by LiCl and A83-01 (*SI Appendix*, Fig. S17*B*), but the nuclear translocation of β-catenin was most evident in the cARLA group (Fig. 5*C*). This was not accompanied by the disruption of junctional β-catenin or VE-cadherin (*SI Appendix*, Fig. S18*A*) complexes, and was consistent with the upregulation of *RAPGEF5*, a mediator of β-catenin nuclear import, by cARLA (Fig. 5*B*). Notably, the effect of cARLA was synergistic (*SI Appendix*, Fig. S17*E*) for 14 out of

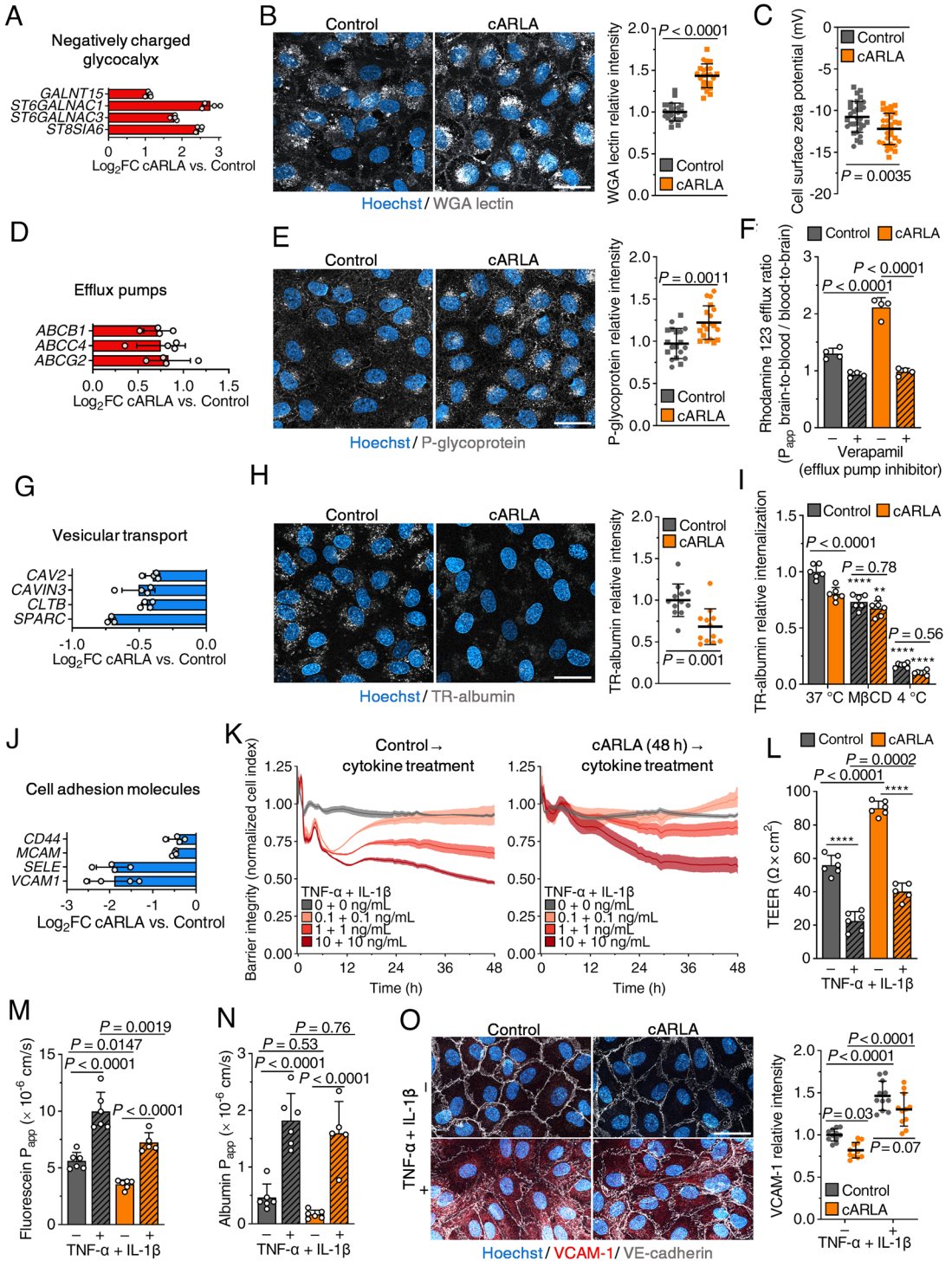

Fig. 4. cARLA induces a complex BBB phenotype at the mRNA, protein, and functional levels in human brain–like ECs. (*A*) Key glycocalyx synthesis enzymes are up-regulated upon cARLA treatment. Mean ± SD. (*B*) Wheat germ agglutinin (WGA) lectin staining labeling negatively charged sialic acid residues in the EC glycocalyx. (Scale bar: 50 μm.) Mean ± SD, unpaired *t* test, $t = 11.43$, $df = 43$, $n = 22$ to 24 from two experiments. (*C*) Cell surface zeta potential measurement in ECs. Mean ± SD, unpaired *t* test, $t = 3.045$, $df = 60$, $n = 31$ from two experiments. (*D*) Key BBB efflux transporters are up-regulated upon cARLA treatment. Mean ± SD. (*E*) P-glycoprotein (P-gp, *ABCB1*) immunostaining in ECs. (Scale bar: 50 μm.) Mean ± SD, unpaired *t* test, $t = 4.065$, $df = 36$, $n = 19$ from two experiments. (*F*) Efflux ratio of rhodamine 123, a ligand of efflux pumps, across the BBB coculture model in the presence or absence of verapamil, an efflux pump inhibitor. Mean ± SD, two-way ANOVA with Bonferroni's post hoc test, $n = 4$. (*G*) Key mediators of endocytic vesicle formation and nonspecific albumin uptake are down-regulated by cARLA. Mean ± SD. (*H*) Texas Red (TR)-labeled albumin internalization in ECs visualized by live cell confocal microscopy. (Scale bar: 50 μm.) Mean ± SD, unpaired *t* test, $t = 3.786$, $df = 22$, $n = 12$. (*I*) TR-albumin internalization in ECs quantified by fluorescent spectrophotometry. MβCD: randomly methylated β-cyclodextrin, an inhibitor of lipid raft/caveolin-mediated endocytosis. Incubation at 4 °C inhibits energy-dependent internalization. Mean ± SD, two-way ANOVA with Bonferroni's post hoc test, $^{**}P < 0.01$, $^{****}P < 0.0001$ compared to its respective 37 °C group, $n = 6$. (*J*) Key immune cell adhesion molecules are down-regulated by cARLA in the absence of inflammatory stimuli. Mean ± SD. (*K*) Barrier integrity of control and cARLA-treated ECs upon TNF-α + IL-1β treatment, measured by impedance. Higher normalized cell index values indicate better-preserved barrier integrity. Mean ± SD, $n = 4$ to 6. (*L*) Measurement of TEER in control and cARLA-treated cocultures upon TNF-α + IL-1β treatment. Mean ± SD, two-way ANOVA with Bonferroni's post hoc test, $^{****}P < 0.0001$ compared to nonstimulated ECs, $n = 6$. (*M*) Permeability of sodium fluorescein and (*N*) Evans blue–albumin across the control or cARLA-treated coculture model upon TNF-α + IL-1β treatment. Mean ± SD, two-way ANOVA with Bonferroni's post hoc test, $n = 5$ to 6. (*O*) VCAM-1 (red) and VE-cadherin (gray) immunostaining in control or cARLA-treated ECs, with or without TNF-α + IL-1β treatment. Mean ± SD, two-way ANOVA with Bonferroni's post hoc test, $n = 11$.

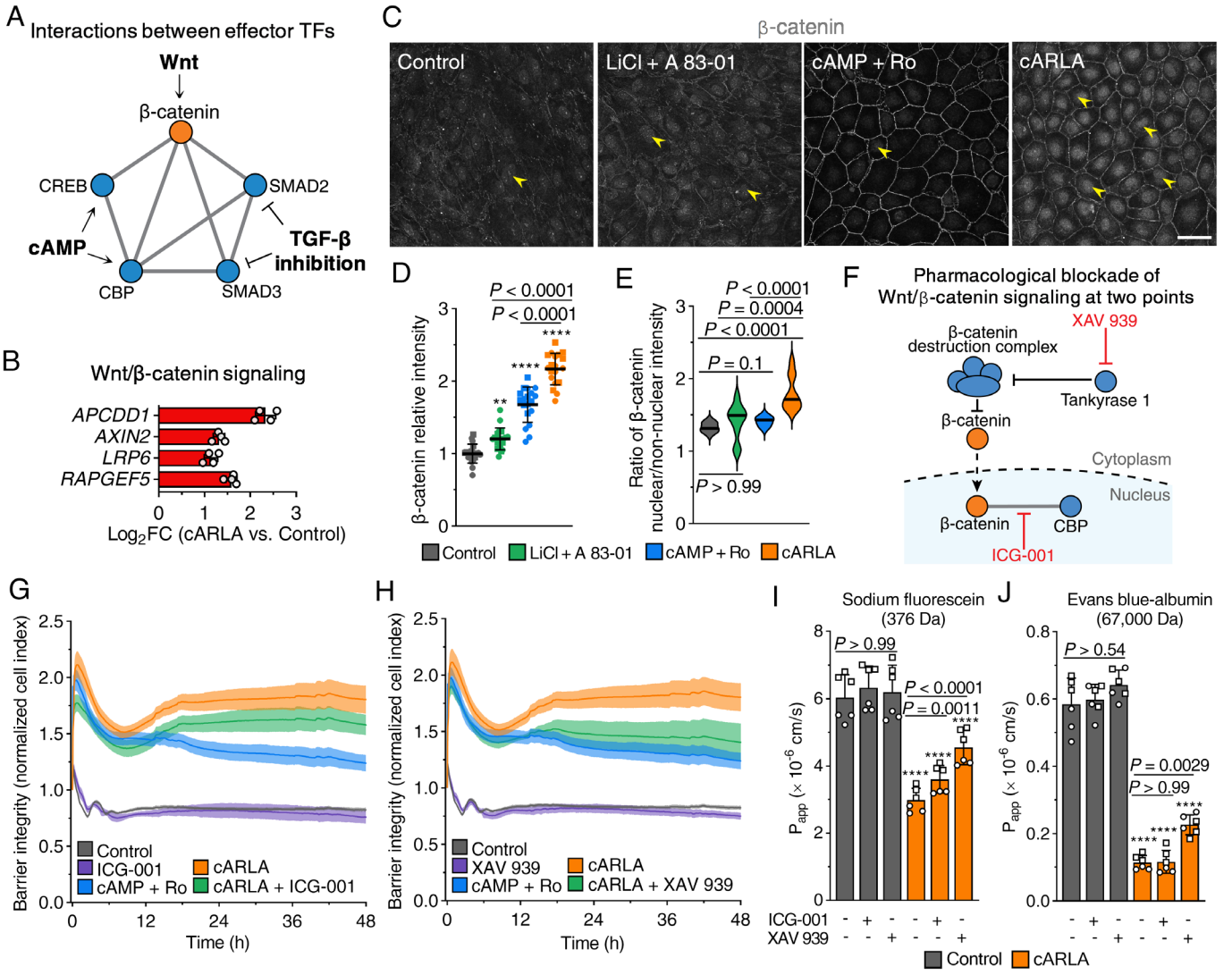

Fig. 5. Targeted pathways converge on Wnt/β-catenin signaling to mediate the effect of cARLA. (*A*) Schematic drawing of known interactions between effector transcription factors (TFs) of cAMP, Wnt, and TGF-β signaling. (*B*) Canonical target genes of Wnt/β-catenin signaling are up-regulated by cARLA. Mean ± SD. (*C*) β-catenin immunostaining in human brain–like ECs. Arrowheads point to nuclear β-catenin, a hallmark of active Wnt signaling. (Scale bar: 50 μm.) (*D*) Quantification of β-catenin staining intensity and (*E*) β-catenin nuclear/non-nuclear ratio. Mean ± SD for intensity, median ± quartiles for nuclear/non-nuclear ratio, ANOVA with Bonferroni's post hoc test, $^{**}P < 0.01$, $^{****}P < 0.0001$ compared to the control group, $n = 20$ from two experiments. (*F*) Schematic drawing of the mechanism of action of Wnt signaling inhibitors ICG-001 and XAV 939. (*G*) Barrier integrity measured by impedance in EC monolayers, with or without ICG-001 (5 μM) and (*H*) XAV 939 (1 μM). Higher normalized cell index values indicate higher barrier integrity. Mean ± SD, $n = 5$ to 6. (*I*) Permeability of sodium fluorescein and (*J*) Evans blue–albumin across the coculture model, with or without ICG-001 and XAV 939. Mean ± SD, ANOVA with Bonferroni's post hoc test. $^{****}P < 0.0001$ in cARLA-treated ECs compared to its respective treatment in the control group, $n = 6$ from two experiments.

the 100 BBB-specific genes in our set, 6 of which are direct targets of Wnt signaling.

To investigate how a highly active state of Wnt/β-catenin signaling contributes to the effect of cARLA, we pharmacologically blocked this pathway at two different points (Fig. 5*F*). ICG-001 specifically inhibits the β-catenin-CREB-binding protein (CBP) interaction in the nucleus, while XAV 939 blocks the pathway upstream of nuclear translocation. We used these inhibitors in concentrations that do not interfere with basal barrier integrity (*SI Appendix*, Fig. S18 *B* and *C*) but block the effect of elevated levels of Wnt signaling on impedance (Fig. 5 *G* and *H*). ICG-001 moderately decreased (Fig. 5*G*), whereas XAV 939 more potently reduced the effect of cARLA on barrier tightness, almost to the level of cAMP+Ro treatment (Fig. 5*H*). By contrast, the elevation in barrier integrity by cAMP+Ro alone was not affected by these inhibitors (*SI Appendix*, Fig. S17 *C* and *D*). Treatment with XAV 939 increased the permeability of both fluorescein and albumin, whereas ICG-001 only increased the permeability of fluorescein but not albumin, across the cARLA-treated coculture model (Fig. 5 *I* and *J*). These findings suggest that the three pathways converge on Wnt/β-catenin signaling to mediate the effect of cARLA on barrier integrity and that specifically, the β-catenin-CBP interaction is involved in establishing paracellular tightness.

cARLA Improves the Prediction of Drug and Nanoparticle Transport across the Human BBB. Finally, to put cARLA into practice, we assessed the penetration of 10 clinically used small-molecule drugs across the coculture model, with or without cARLA treatment. Drugs were selected to represent different routes of penetration across the BBB, such as passive diffusion, efflux, and influx transport (*SI Appendix*, Tables S4 and S5). In blood-to-brain direction, the permeability of efflux pump ligands vinblastine,

loperamide, salicylic acid, and verapamil was lower upon cARLA treatment (Fig. 6*A*). Conversely, cARLA increased the permeability of tacrine (influx transport) and propranolol (passive diffusion, influx transport) across the coculture model. As a consequence, the cARLA-treated human BBB model could correctly discriminate between drugs that readily enter the central nervous system in vivo and those that do not (Fig. 6*A*). Treatment with cARLA also elevated the efflux ratio of loperamide and methotrexate, indicating an improved vectorial transport across the BBB model (Fig. 6*B*). We observed similar results regarding the extent of drug penetration (Fig. 6*C*) given as in vitro unbound brain-to-plasma partition coefficients ($K_{p,uu,brain}$) (22, 25, 57). Importantly, cARLA increased the overall correlation between human in vitro $K_{p,uu,brain}$ values and in vivo brain penetration data from rats (57) and nonhuman primates (58) (Fig. 6*D*). In the case of verapamil, the only drug on our list with human clinical $K_{p,uu,brain}$ data available, the cARLA-treated BBB model closely approximated the human in vivo value (Fig. 6*E* and *SI Appendix*, Fig. S19*A*), being second only to nonhuman primate in vivo data among predictive models. In cases of drugs where no human clinical data were available, we selected nonhuman primate values as reference points. For all drugs in this group, cARLA shifted in vitro $K_{p,uu,brain}$ values toward nonhuman primate in vivo values, compared to the control BBB model (*SI Appendix*, Fig. S19*B*).

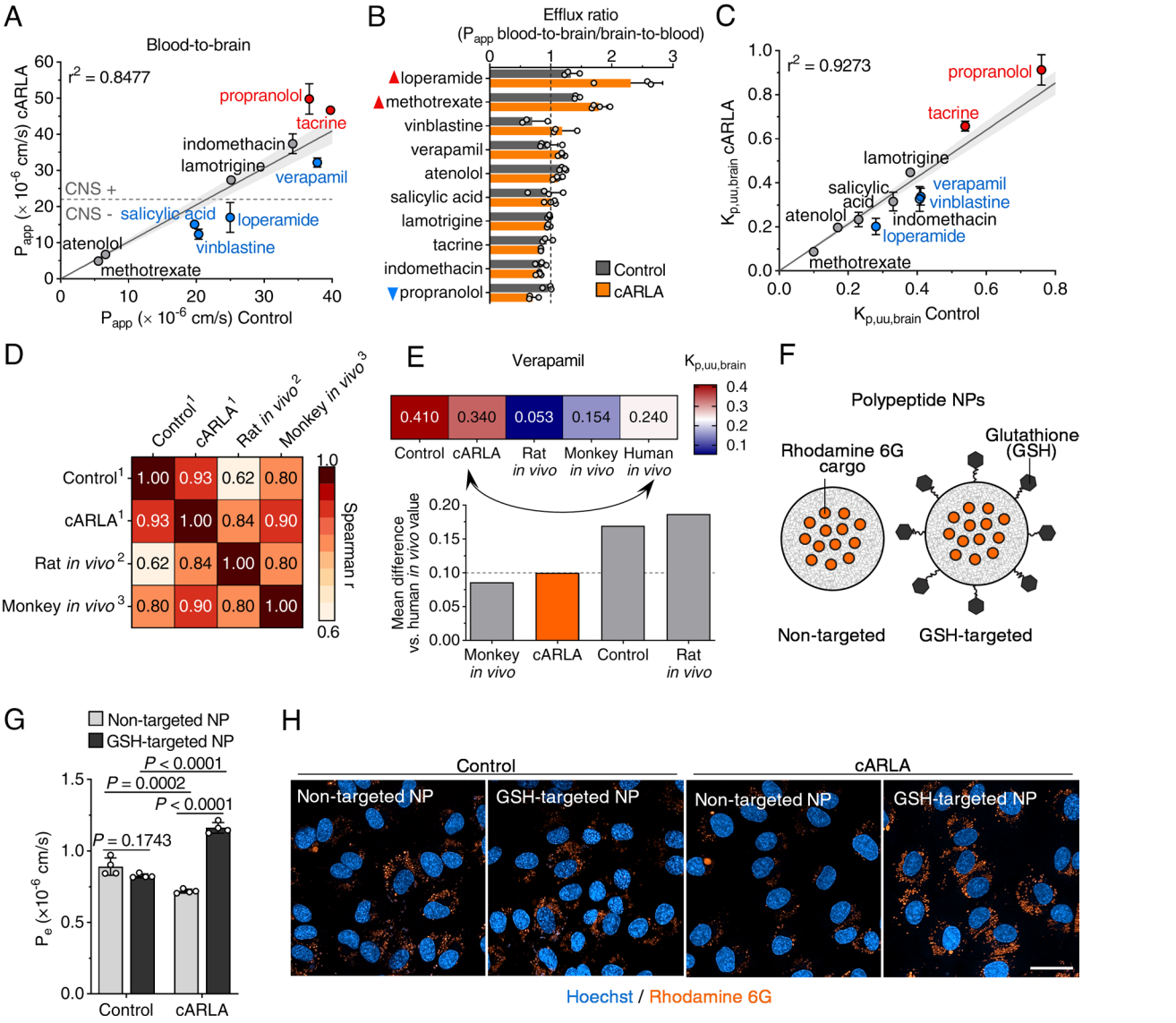

Fig. 6. cARLA improves the in vitro prediction of drug and nanoparticle delivery across the human BBB. (*A*) Permeability of 10 clinically used drugs in blood-to-brain direction across the human brain–like EC-PC coculture model, with or without cARLA treatment. CNS: central nervous system. Red and blue color indicates higher and lower permeability, respectively, for a given drug upon cARLA treatment ($P < 0.05$). Mean ± SD for symbols, $n = 3$ to 4. Line of best fit with 95% CIs and R^2 value from a simple linear regression are shown. (*B*) Drug efflux ratios in the coculture model. Mean ± SD, multiple unpaired *t* tests with Welch's correction, $n = 3$ to 4. Upward red and downward blue triangles indicate higher and lower efflux ratios, respectively ($P < 0.05$). (*C*) In vitro unbound brain-to-plasma partition coefficient ($K_{p,uu,brain}$) of drugs across the coculture model, with or without cARLA treatment. Red and blue color indicates higher and lower values, respectively, for a given drug upon cARLA treatment ($P < 0.05$). Mean ± SD for symbols, $n = 3$ to 4. Line of best fit with 95% CIs and R^2 value from a simple linear regression are shown. (*D*) Correlation heatmap of in vitro $K_{p,uu,brain}$ values for the whole set of drugs from our experiments with in vivo $K_{p,uu,brain}$ data from rats and nonhuman primates. Numbers inside boxes are Spearman's correlation coefficients. Data were obtained from [1]present study, [2]Fridén et al. (57), and [3]Sato et al. (58). (*E*) Comparison of $K_{p,uu,brain}$ measured in vivo in humans with its predictive models for the drug verapamil. *Upper* panel: Heat map of $K_{p,uu,brain}$ values. *Lower* panel: Mean difference of $K_{p,uu,brain}$ values compared to human in vivo data. Lower values indicate better prediction. (*F*) Schematic drawing of nontargeted and GSH-targeted polypeptide nanoparticles (NPs) carrying rhodamine 6G cargo. (*G*) Permeability of nontargeted and GSH-targeted NPs across the coculture BBB model, with or without cARLA treatment. P_e: endothelial permeability coefficient. Mean ± SD, two-way ANOVA with Bonferroni's post hoc test, $n = 4$. (*H*) Internalization of nontargeted and GSH-targeted NPs carrying rhodamine 6G cargo (orange) in ECs, visualized by live cell confocal microscopy. (Scale bar: 50 μm.)

We also tested the effect of cARLA on the penetration of brain-targeted nanocarriers by assessing the permeability of polypeptide nanoparticles (NPs) decorated with or without the BBB-specific targeting ligand glutathione (59–61) (GSH; Fig. 6*F*). In agreement with lower basal levels of endocytosis upon cARLA treatment (Fig. 4 *G–I*), the permeability of nontargeted NPs was lower across the cARLA-treated BBB model compared to the control group (Fig. 6*G*). Notably, the BBB-specific targeting effect of GSH was apparent in the cARLA-treated but not in the control model, based on both the permeability (Fig. 6*G*) and internalization of NPs in ECs (Fig. 6*H*). Taken together, our results demonstrate that by inducing several aspects of BBB function, cARLA can improve the in vitro prediction of therapeutic drug and NP transport across the human BBB.

Discussion

In the past decade, several laboratories established BBB models derived from human stem cells (11–25). Not only can this technology revolutionize drug development for the human brain by eliminating problems with species differences, it can also provide mechanistic insight into how the human BBB functions in health and disease. However, state-of-the-art human BBB models either have high barrier tightness but suffer from a mixed epithelial–endothelial identity or the cells are vascular ECs but have weak barrier properties (26, 27). This is a major limitation and thus, there is consensus in the field that existing differentiation protocols need serious improvements to better mimic both the endothelial nature and the complexity of the human BBB (26, 62–64). In this study, we describe an efficient, reproducible yet easy-to-use approach to induce complex BBB properties in vascular ECs in vitro.

The small-molecule cocktail cARLA, which consists of pCPT-cAMP+Ro-20-1724+LiCl+A83-01, simultaneously activates cAMP and Wnt/β-catenin signaling and inhibits the TGF-β pathway. So far, soluble factors targeting these pathways have been separately used to elevate BBB tightness in vitro. For example, cAMP-elevating agents (pCPT-cAMP, Ro-20-1724, and forskolin) rapidly increased junctional integrity in bovine and rodent primary brain ECs (47, 48, 65). The activation of Wnt/β-catenin signaling (22, 40–43) by Wnt ligands (Wnt-3a and Wnt-7a/b) or small molecules (LiCl, 6-BIO, and CHIR99021) as well as the inhibition of TGF-β signaling by receptor antagonists (RepSox and A83-01) (44, 45) have also been shown to induce a subset of barrier properties individually. Yet we and others hypothesized that signaling cues do not act separately in ECs but rather interact with one another during BBB maturation. Indeed, overexpression of a combination of general and brain EC-specific transcription factors has been shown to increase barrier integrity in stem cell–derived ECs by ~40% (65). In contrast to targeting signaling pathways separately, Praça et al. used Wnt-3a, VEGF, and retinoic acid to simultaneously activate multiple pathways during EC differentiation (15). These factors, however, did not effectively potentiate each others' effect on barrier tightness (11). The strength of our approach compared to previous studies is that we performed a combinatorial screen of selected compounds for their ability to increase barrier tightness in ECs. This allowed us to identify a link between cAMP, Wnt/β-catenin, and TGF-β signaling at the BBB in vitro and thus, we could rationally develop a small-molecule cocktail with optimal composition to target this interaction. Treatment with cARLA has a greater than twofold, synergistic effect on barrier tightness via claudin-5, the dominant tight junction protein at the BBB (66). Based on our results, cARLA not only increases claudin-5 expression but can also promote its localization and stabilization at the intercellular junctions. We further support these findings by showing that the effect of cARLA is mediated by a convergence of targeted pathways on Wnt/β-catenin signaling.

The other main strength of our approach is that cARLA induces several aspects of BBB function, not just junctional tightness. Recapitulating these different BBB properties in vitro is necessary for both physiological studies and to predict the penetration of drugs and nanocarriers across the BBB. However, the induction of a complex BBB phenotype has remained challenging in human stem cell–derived vascular ECs using current differentiation protocols (15, 21, 22, 27). Notably, cARLA does not induce epithelial-associated genes, and cARLA-treated ECs retain their characteristic endothelial response to proinflammatory cytokines. We also demonstrate that cARLA up-regulates 39 to 45% of BBB-specific genes, and shifts the gene expressional profile of human stem cell–derived ECs toward the in vivo brain endothelial signature. As a limitation, 10 out of the selected 100 BBB-specific genes, including transcription factors *LEF1*, *FOXF2,* and *ZIC3*, were not expressed in human brain–like ECs and could not be induced by cARLA. Treatment with our small-molecule cocktail also did not elevate the expression of 45 other BBB-specific genes, such as *MFSD2A* or *SLC38A5* (SNAT5). By contrast, cARLA induced a higher glycocalyx density and efflux pump activity as well as lower rates of transcytosis, which we validated at mRNA, protein, and functional levels. Recapitulating these BBB properties in vitro is important as pathological factors modify, and therapeutics interact with the EC glycocalyx, influx and efflux transporters as well as transcytotic pathways at the BBB. Accordingly, we observed a higher in vitro–in vivo correlation, and a substantially better prediction of the penetration of clinically used small-molecule drugs in the cARLA-treated human BBB model compared to the control group and previously published human in vitro models. Among these, the effect of cARLA was best seen for drugs that are efflux pump ligands or have an influx transport mechanism across the BBB. Our data also indicate that cARLA increases the paracellular tightness of the human BBB model to a level that is suitable for testing larger biopharmaceuticals, such as antibody constructs, enzymes, and brain-targeted NPs.

Importantly, the aim of our study was not to establish a new human BBB model but rather to create an approach that can be used in a range of models across laboratories to move the field forward. To this end, we selected commercially available small-molecules as an easy, affordable, and rapid way to target developmentally relevant signaling pathways. Our method uses a single "hit-and-run" treatment with cARLA for 24 to 48 h to induce barrier maturation in ECs before the cells can be used in experiments. Notably, the effect of cARLA on barrier tightness is maintained after removal of the treatment, which can be important for several experimental setups. Whether the efficacy of cARLA can be further improved by other cues such as fluid flow and organ-on-a-chip technology (6, 19, 67), 3D microenvironment (68) or basement membrane composition (69) remains to be explored. As we are aware of current difficulties in the field related to the induction of BBB properties of culture models in a reproducible way, we demonstrated the consistent effect of cARLA treatment using different batches of cells, measured by different experts in our research group. Moreover, we verified the effectiveness of cARLA in additional, well-established BBB models, namely EECM-BMEC-like cells differentiated from human induced pluripotent stem cells (21), the mouse brain EC line bEnd.3 and primary brain EC-PC-AC coculture models (51) from mice and rats. Although it is a limitation of our study that the interaction between the three pathways targeted by cARLA was not yet proven in vivo, the synergistic effect of cARLA is conserved between species and is reproducible across BBB models of different complexity.

Due to its high efficacy, reproducibility, and ease of use, cARLA has the potential to be applied in a variety of BBB culture models across laboratories to advance drug development for the human brain. We envision that our study will also boost future research in understanding interactions between signaling pathways that govern the formation, maturation, and maintenance of the BBB.

Materials and Methods

Derivation and culture of human stem cell–derived ECs, impedance-based measurement of barrier integrity, optimal concentrations of soluble factors and cARLA in human ECs, construction of the human brain–like EC and bovine brain PC coculture BBB model, the measurement of transendothelial electrical resistance, tracer permeability, immunocytochemistry and image analysis, differentiation and culture of EECM-BMEC-like cells and SMLCs, animals, assembly of the primary mouse brain EC-PC-AC coculture BBB model, the mouse brain endothelial cell line bEnd.3, assembly of the primary rat brain EC-PC-AC coculture BBB model, total RNA isolation, library preparation and 3′ RNA-sequencing (MACE-seq), bioinformatic analysis of MACE-seq data, glycocalyx staining and measurement of cell surface charge, measurement of efflux pump activity, western blotting, measurement of albumin internalization, measurement of barrier integrity in response to inflammation, pharmacological inhibition of Wnt/β-catenin signaling, penetration of small-molecule drugs across the human brain–like EC-PC BBB model, synthesis and penetration of nanoparticles across the human brain–like EC-PC BBB model, and statistics are described in *SI Appendix, Materials and Methods*.

Data, Materials, and Software Availability. MACE-seq data generated and analyzed in this study have been deposited to the Gene Expression Omnibus (GEO) repository under accession number GSE224846 (70). Source data are provided with the manuscript and on Dryad: https://datadryad.org/stash/share/9j1-8dVQt4EMgoKBMV-OoZfcRzmUPQSuOIvIlsdUOKQ. All other data are included in the manuscript and/or *SI Appendix*.

ACKNOWLEDGMENTS. Prof. Christer Betsholtz and Dr. Maarja A. Mäe (Uppsala University, Sweden) are gratefully acknowledged for providing the *Cldn5*$^{+/-}$ mice. We are grateful to Dr. Hideaki Nishihara and Dr. Kinya Matsuo (Yamaguchi University, Japan) for their guidance on iPSC-derived EECM-BMEC-like cells. We thank the technical assistance of Katalin Kokavszky and Csilla Kovács (HUN-REN BRC) in the experiments. We are also grateful to Dr. Imola Wilhelm, Dr. István Krizbai, and Dr. Tibor Páli (HUN-REN BRC) for the use of a CellZScope+ instrument and a Horiba Jobin-Yvon Fluorolog 3 spectrofluorometer. This work was funded by the National Research, Development and Innovation Office of Hungary (K143766 to M.A.D. and FK143233 to S.V.) and the Hungarian Academy of Sciences (NAP2022-I-6/2022 to M.A.D.). The Campbell Lab is supported by grants from SFI (Eye-D-21/SPP/3732), Enterprise Ireland, and The Irish Research Council (IRC), by a grant from SFI (16/RC/3948) cofunded under the European Regional Development fund by FutureNeuro industry partners, and by a European Research Council (ERC) grant, "Retina-Rhythm" (864522). G.P. was supported by the National Academy of Scientist Education Program of the National Biomedical Foundation under the sponsorship of the Hungarian Ministry of Culture and Innovation. M.M. was supported by the National Research, Development and Innovation Office of Hungary (PD138930). F.R.W. was supported by the Secretariat of Lorand Eotvos Research Network (SA-111/2021).

Author affiliations: [a]Institute of Biophysics, Biological Research Centre, Hungarian Research Network, Szeged H-6726, Hungary; [b]Doctoral School of Biology, University of Szeged, Szeged H-6720, Hungary; [c]GenXPro GmbH, Frankfurt am Main 60438, Germany; [d]In Vitro Metabolism Laboratory, Gedeon Richter, Budapest H-1103, Hungary; [e]Department of Chemical Engineering, National Cheng Kung University, Tainan 70101, Taiwan; [f]Laboratoire de la Barriére Hémato-Encéphalique, Université d'Artois, Lens 62307, France; [g]Institute of Genetics, Biological Research Centre, Hungarian Research Network, Szeged H-6726, Hungary; and [h]Smurfit Institute of Genetics, Trinity College Dublin, Dublin D02 VF25, Ireland

Author contributions: G.P. and M.A.D. designed research; G.P., M.M., A.S., J.P.V., F.R.W., R.F., I.K., Z.H., I.G., and S.V. performed research; G.V., J.-S.J., F.G., M.K.P., M.V., N.H., and M.C. contributed new reagents/analytic tools; G.P., M.M., A.S., J.P.V., F.R.W., R.F., I.K., Z.H., G.V., I.G., S.V., and M.A.D. analyzed data; and G.P., M.M., A.S., J.P.V., F.R.W., R.F., I.K., Z.H., G.V., I.G., J.-S.J., F.G., M.K.P., M.V., N.H., M.C., S.V., and M.A.D. wrote the paper.

1. B. V. Zlokovic, The blood-brain barrier in health and chronic neurodegenerative disorders. *Neuron* **57**, 178–201 (2008).
2. N. J. Abbott, A. A. Patabendige, D. E. Dolman, S. R. Yusof, D. J. Begley, Structure and function of the blood-brain barrier. *Neurobiol. Dis.* **37**, 13–25 (2010).
3. W. M. Pardridge, Drug transport across the blood-brain barrier. *J. Cereb. Blood Flow Metab.* **32**, 1959–1972 (2012).
4. R. N. Munji *et al.*, Profiling the mouse brain endothelial transcriptome in health and disease models reveals a core blood-brain barrier dysfunction module. *Nat. Neurosci.* **22**, 1892–1902 (2019).
5. M. D. Sweeney, Z. Zhao, A. Montagne, A. R. Nelson, B. V. Zlokovic, Blood-brain barrier: From physiology to disease and back. *Physiol. Rev.* **99**, 21–78 (2019).
6. D. E. Ingber, Human organs-on-chips for disease modelling, drug development and personalized medicine. *Nat. Rev. Genet.* **23**, 467–491 (2022).
7. H. C. Helms *et al.*, In vitro models of the blood-brain barrier: An overview of commonly used brain endothelial cell culture models and guidelines for their use. *J. Cereb. Blood Flow Metab.* **36**, 862–890 (2016).
8. Y. Uchida *et al.*, Quantitative targeted absolute proteomics of human blood-brain barrier transporters and receptors. *J. Neurochem.* **117**, 333–345 (2011).
9. R. Shawahna *et al.*, Transcriptomic and quantitative proteomic analysis of transporters and drug metabolizing enzymes in freshly isolated human brain microvessels. *Mol. Pharm.* **8**, 1332–1341 (2011).
10. Y. Uchida *et al.*, Comparison of absolute protein abundances of transporters and receptors among blood-brain barriers at different cerebral regions and the blood-spinal cord barrier in humans and rats. *Mol. Pharm.* **17**, 2006–2020 (2020).
11. E. S. Lippmann *et al.*, Derivation of blood-brain barrier endothelial cells from human pluripotent stem cells. *Nat. Biotechnol.* **30**, 783–791 (2012).
12. E. S. Lippmann, A. Al-Ahmad, S. M. Azarin, S. P. Palecek, E. V. Shusta, A retinoic acid-enhanced, multicellular human blood-brain barrier model derived from stem cell sources. *Sci. Rep.* **4**, 4160 (2014).
13. S. G. Canfield *et al.*, An isogenic blood-brain barrier model comprising brain endothelial cells, astrocytes, and neurons derived from human induced pluripotent stem cells. *J. Neurochem.* **140**, 874–888 (2017).
14. A. Appelt-Menzel *et al.*, Establishment of a human blood-brain barrier co-culture model mimicking the neurovascular unit using induced pluri- and multipotent stem cells. *Stem. Cell Rep.* **8**, 894–906 (2017).
15. C. Praça *et al.*, Derivation of brain capillary-like endothelial cells from human pluripotent stem cell-derived endothelial progenitor cells. *Stem. Cell Rep.* **13**, 599–611 (2019).
16. M. J. Stebbins *et al.*, Human pluripotent stem cell-derived brain pericyte-like cells induce blood-brain barrier properties. *Sci. Adv.* **5**, eaau7375 (2019).
17. T. Qian *et al.*, Directed differentiation of human pluripotent stem cells to blood-brain barrier endothelial cells. *Sci. Adv.* **3**, e1701679 (2017).
18. G. D. Vatine *et al.*, Human iPSC-derived blood-brain barrier chips enable disease modeling and personalized medicine applications. *Cell Stem Cell* **24**, 995–1005.e1006 (2019).
19. T. E. Park *et al.*, Hypoxia-enhanced blood-brain barrier chip recapitulates human barrier function and shuttling of drugs and antibodies. *Nat. Commun.* **10**, 2621 (2019).
20. R. M. Linville *et al.*, Human iPSC-derived blood-brain barrier microvessels: Validation of barrier function and endothelial cell behavior. *Biomaterials* **190–191**, 24–37 (2019).
21. H. Nishihara *et al.*, Advancing human induced pluripotent stem cell-derived blood-brain barrier models for studying immune cell interactions. *Faseb J.* **34**, 16693–16715 (2020).
22. R. Cecchelli *et al.*, A stable and reproducible human blood-brain barrier model derived from hematopoietic stem cells. *PLoS One* **9**, e99733 (2014).
23. A. Mossu *et al.*, A silicon nanomembrane platform for the visualization of immune cell trafficking across the human blood-brain barrier under flow. *J. Cereb. Blood Flow Metab.* **39**, 395–410 (2019).
24. C. Deligne *et al.*, Development of a human in vitro blood-brain tumor barrier model of diffuse intrinsic pontine glioma to better understand the chemoresistance. *Fluids Barriers CNS* **17**, 37 (2020).
25. E. L. J. Moya *et al.*, Miniaturization and automation of a human in vitro blood-brain barrier model for the high-throughput screening of compounds in the early stage of drug discovery. *Pharmaceutics* **13**, 892 (2021).
26. E. S. Lippmann, S. M. Azarin, S. P. Palecek, E. V. Shusta, Commentary on human pluripotent stem cell-based blood-brain barrier models. *Fluids Barriers CNS* **17**, 64 (2020).
27. T. M. Lu *et al.*, Pluripotent stem cell-derived epithelium misidentified as brain microvascular endothelium requires ETS factors to acquire vascular fate. *Proc. Natl. Acad. Sci. U.S.A.* **118**, e2016950118 (2021).
28. A. Armulik *et al.*, Pericytes regulate the blood-brain barrier. *Nature* **468**, 557–561 (2010).
29. R. Daneman, L. Zhou, A. A. Kebede, B. A. Barres, Pericytes are required for blood-brain barrier integrity during embryogenesis. *Nature* **468**, 562–566 (2010).
30. M. D. Sweeney, S. Ayyadurai, B. V. Zlokovic, Pericytes of the neurovascular unit: Key functions and signaling pathways. *Nat. Neurosci.* **19**, 771–783 (2016).
31. R. C. Janzer, M. C. Raff, Astrocytes induce blood-brain barrier properties in endothelial cells. *Nature* **325**, 253–257 (1987).
32. M. Simard, G. Arcuino, T. Takano, Q. S. Liu, M. Nedergaard, Signaling at the gliovascular interface. *J. Neurosci.* **23**, 9254–9262 (2003).
33. N. J. Abbott, L. Rönnbäck, E. Hansson, Astrocyte-endothelial interactions at the blood-brain barrier. *Nat. Rev. Neurosci.* **7**, 41–53 (2006).
34. J. M. Stenman *et al.*, Canonical Wnt signaling regulates organ-specific assembly and differentiation of CNS vasculature. *Science* **322**, 1247–1250 (2008).
35. R. Daneman *et al.*, Wnt/beta-catenin signaling is required for CNS, but not non-CNS, angiogenesis. *Proc. Natl. Acad. Sci. U.S.A.* **106**, 641–646 (2009).
36. B. Vanhollebeke *et al.*, Tip cell-specific requirement for an atypical Gpr124- and Reck-dependent Wnt/β-catenin pathway during brain angiogenesis. *Elife* **4**, e06489 (2015).

37. S. Liebner *et al.*, Wnt/beta-catenin signaling controls development of the blood-brain barrier. *J. Cell Biol.* **183**, 409–417 (2008).
38. M. Cullen *et al.*, GPR124, an orphan G protein-coupled receptor, is required for CNS-specific vascularization and establishment of the blood-brain barrier. *Proc. Natl. Acad. Sci. U.S.A.* **108**, 5759–5764 (2011).
39. Y. Zhou *et al.*, Canonical WNT signaling components in vascular development and barrier formation. *J. Clin. Invest.* **124**, 3825–3846 (2014).
40. R. Paolinelli *et al.*, Wnt activation of immortalized brain endothelial cells as a tool for generating a standardized model of the blood brain barrier in vitro. *PLoS One* **8**, e70233 (2013).
41. B. Weksler, I. A. Romero, P. O. Couraud, The hCMEC/D3 cell line as a model of the human blood brain barrier. *Fluids Barriers CNS* **10**, 16 (2013).
42. M. D. Laksitorini, V. Yathindranath, W. Xiong, S. Hombach-Klonisch, D. W. Miller, Modulation of Wnt/β-catenin signaling promotes blood-brain barrier phenotype in cultured brain endothelial cells. *Sci. Rep.* **9**, 19718 (2019).
43. B. D. Gastfriend *et al.*, Wnt signaling mediates acquisition of blood-brain barrier properties in naïve endothelium derived from human pluripotent stem cells. *Elife* **10**, e70992 (2021).
44. F. Roudnicky *et al.*, Inducers of the endothelial cell barrier identified through chemogenomic screening in genome-edited hPSC-endothelial cells. *Proc. Natl. Acad. Sci. U.S.A.* **117**, 19854–19865 (2020).
45. M. Yamashita, H. Aoki, T. Hashita, T. Iwao, T. Matsunaga, Inhibition of transforming growth factor beta signaling pathway promotes differentiation of human induced pluripotent stem cell-derived brain microvascular endothelial-like cells. *Fluids Barriers CNS* **17**, 36 (2020).
46. L. L. Rubin *et al.*, A cell culture model of the blood-brain barrier. *J. Cell Biol.* **115**, 1725–1735 (1991).
47. H. Wolburg *et al.*, Modulation of tight junction structure in blood-brain barrier endothelial cells. Effects of tissue culture, second messengers and cocultured astrocytes. *J. Cell Sci.* **107**, 1347–1357 (1994).
48. M. A. Deli, M. P. Dehouck, C. S. Abrahám, R. Cecchelli, F. Joó, Penetration of small molecular weight substances through cultured bovine brain capillary endothelial cell monolayers: The early effects of cyclic adenosine 3',5'-monophosphate. *Exp. Physiol.* **80**, 675–678 (1995).
49. M. Vanlandewijck *et al.*, A molecular atlas of cell types and zonation in the brain vasculature. *Nature* **554**, 475–480 (2018).
50. S. Guérit *et al.*, Astrocyte-derived Wnt growth factors are required for endothelial blood-brain barrier maintenance. *Prog. Neurobiol.* **199**, 101937 (2021).
51. S. Nakagawa *et al.*, A new blood-brain barrier model using primary rat brain endothelial cells, pericytes and astrocytes. *Neurochem. Int.* **54**, 253–263 (2009).
52. M. F. Sabbagh *et al.*, Transcriptional and epigenomic landscapes of CNS and non-CNS vascular endothelial cells. *Elife* **7**, e36187 (2018).
53. A. C. Yang *et al.*, A human brain vascular atlas reveals diverse mediators of Alzheimer's risk. *Nature* **603**, 885–892 (2022).
54. F. J. Garcia *et al.*, Single-cell dissection of the human brain vasculature. *Nature* **603**, 893–899 (2022).
55. H. W. Song *et al.*, Transcriptomic comparison of human and mouse brain microvessels. *Sci. Rep.* **10**, 12358 (2020).
56. J. Schaffenrath *et al.*, Blood-brain barrier alterations in human brain tumors revealed by genome-wide transcriptomic profiling. *Neuro. Oncol.* **23**, 2095–2106 (2021).
57. M. Fridén *et al.*, Structure-brain exposure relationships in rat and human using a novel data set of unbound drug concentrations in brain interstitial and cerebrospinal fluids. *J. Med. Chem.* **52**, 6233–6243 (2009).
58. S. Sato, K. Matsumiya, K. Tohyama, Y. Kosugi, Translational CNS steady-state drug disposition model in rats, monkeys, and humans for quantitative prediction of brain-to-plasma and cerebrospinal fluid-to-plasma unbound concentration ratios. *Aaps J.* **23**, 81 (2021).
59. J. Rip *et al.*, Glutathione PEGylated liposomes: Pharmacokinetics and delivery of cargo across the blood-brain barrier in rats. *J. Drug Target* **22**, 460–467 (2014).
60. D. Maussang *et al.*, Glutathione conjugation dose-dependently increases brain-specific liposomal drug delivery in vitro and in vivo. *Drug Discov. Today Technol.* **20**, 59–69 (2016).
61. T. Fekete *et al.*, Optically manipulated microtools to measure adhesion of the nanoparticle-targeting ligand glutathione to brain endothelial cells. *ACS Appl. Mater. Interfaces* **13**, 39018–39029 (2021).
62. M. J. Workman, C. N. Svendsen, Recent advances in human iPSC-derived models of the blood-brain barrier. *Fluids Barriers CNS* **17**, 30 (2020).
63. R. M. Linville, P. C. Searson, Next-generation in vitro blood-brain barrier models: Benchmarking and improving model accuracy. *Fluids Barriers CNS* **18**, 56 (2021).
64. T. M. Lu *et al.*, Human induced pluripotent stem cell-derived brain endothelial cells: Current controversies. *Front. Physiol.* **12**, 642812 (2021).
65. F. Roudnicky *et al.*, Identification of a combination of transcription factors that synergistically increases endothelial cell barrier resistance. *Sci. Rep.* **10**, 3886 (2020).
66. C. Greene, N. Hanley, M. Campbell, Claudin-5: Gatekeeper of neurological function. *Fluids Barriers CNS* **16**, 3 (2019).
67. A. R. Santa-Maria *et al.*, Flow induces barrier and glycocalyx-related genes and negative surface charge in a lab-on-a-chip human blood-brain barrier model. *J. Cereb. Blood Flow. Metab.* **41**, 2201–2215 (2021).
68. R. M. Linville *et al.*, Three-dimensional microenvironment regulates gene expression, function, and tight junction dynamics of iPSC-derived blood-brain barrier microvessels. *Fluids Barriers CNS* **19**, 87 (2022).
69. J.-W. Choi, J. Youn, D. S. Kim, T.-E. Park, Human iPS-derived blood-brain barrier model exhibiting enhanced barrier properties empowered by engineered basement membrane. *Biomaterials* **293**, 121983 (2023).
70. G. Porkoláb *et al.*, Data from "Synergistic induction of blood-brain barrier properties." Gene Expression Omnibus (GEO). https://www.ncbi.nlm.nih.gov/geo/query/acc.cgi?acc=GSE224846. Deposited 8 February 2023.